Journal of Industrial and Engineering Chemistry 127 (2023) 579–589

Contents lists available at ScienceDirect

Journal of Industrial and Engineering Chemistry

journal homepage: www.elsevier.com/locate/jiec

Tailoring optical constants of few-layer black phosphorus coatings: Spectroscopic ellipsometry approach supported by *ab-initio* simulation

Aleksandra Wieloszyńska [a], Krzysztof Pyrchla [a], Paweł Jakóbczyk [a], Dawid Lentka [a], Mirosław Sawczak [b], Łukasz Skowroński [c], Robert Bogdanowicz [a,*]

[a] Faculty of Electronics, Telecommunications and Informatics, Gdańsk University of Technology, Narutowicza 11/12, 80-233 Gdańsk, Poland
[b] Polish Academy of Sciences, The Szewalski Institute of Fluid-Flow Machinery, The Centre for Plasma and Laser Engineering, Fiszera 14, 80-231 Gdańsk, Poland
[c] Bydgoszcz University of Science and Technology, 7 Al. Prof. S. Kaliskiego St., 85-796 Bydgoszcz, Poland

ARTICLE INFO

Article history:
Received 3 May 2023
Revised 17 July 2023
Accepted 19 July 2023
Available online 23 July 2023

Keywords:
Black Phosphorus
Two-Dimensional
Optical Properties
Spectroscopic Ellipsometry
Density-Functional Theory

ABSTRACT

2D black phosphorus (BP) has attracted extensive attention as an anisotropic platform for novel optoelectronic and polarizing optics applications. Insight into the factors that tune the optical and polarizing properties of 2D BP reveals their essential influence on BP-based photonic and optoelectronic devices. In this work, studies of the optical constants of few-layer black phosphorus coatings are studied and discussed, with particular emphasis on the complex dielectric function. Herein, the complex optical constants of multi-flake composite films in the energy range of 1.38–6.2 eV by spectroscopic ellipsometry with the use of the classical optical model have been determined. Classical optical simulations were supplied by dielectric function estimations delivered by density functional theory. Additionally, few-layer black phosphorus coatings were imaged by polarizing microscopy and investigated by Raman spectroscopy, revealing a size-tunable flake composition. The pattern analysis of the polarization images reveals a shift in polarization anisotropy originated mainly from the central region of the flake. The semi-isotropic optical properties suggest that the extinction coefficient of BP flakes defines the applications of BP in photonics, waveguides, and directional optoelectronic devices.

Introduction

In the last dozen or so years, two-dimensional (2D) materials such as transition metal dichalcogenides (TMDCs) [1], hexagonal boron nitride (BN) [2], perovskites [3], graphene [4], silicene [5], germanene [6], and phosphorene [7,8] have captured the interest of scientists as promising materials for future electronic and optical applications [9–12]. Of these, since 2014, phosphorene has expanded the homoatomic family of 2D materials. Phosphorene forms a puckered monolayer of black phosphorus in which each phosphorus atom is covalently bonded to the three nearest neighboring atoms of phosphorus [13]. The unique lattice structure of phosphorene gives it special electronic and optoelectronic properties, such as a direct bandgap from 0.3 to 2 eV [14], moderate on/off ratio (10^4–10^5) [15,16] and high carrier mobility (up to 1000 $cm^2 V^{-1} s^{-1}$ at room temperature for a thickness of ca. 10 nm) [17], and anisotropy of its electrical, optical [18,19], magnetic, and electrochemical properties [20]. Monolayer and few-layer black phosphorus (FLBP) [21] have received much attention for their use in nanodevices such as field-effect transistors [22], photovoltaics or photodetectors [12], phototransistors [23], nanoelectromechanical resonators [24], sensors [9,11], and energy storage devices (batteries, supercapacitors) [25]. These features place phosphorene in an interesting position compared to the previously known 2D materials. The bandgap of FLBP can be changed over a wide range, while graphene and TMDCs have bandgaps of 0 eV and 1–2 eV [1,26], respectively. It also influences FLBP's ability to absorb light in a broad range of the spectrum. Furthermore, as was mentioned, phosphorene is strongly anisotropic. For zig-zag-polarized light, FLBP is almost transparent for low energies up to 2.8 eV, at which point the absorption increases significantly, while it is characterized by non-zero absorption between 1.1 eV and 2.8 eV in the armchair direction. This makes FLBP an ideal candidate for optical polarizers [27–29]. Moreover, the absorption of FLBP strongly depends on the number of layers, but, in contrast to other 2D materials such as MoS_2 [30], with decreasing thickness, the absorption increases [31]. Other optical parameters of FLBP also change according to the thickness. Ross *et al* [32] reported differences in the refractive index for 1 to 5 layers, and for bulk BP.

* Corresponding author.
E-mail address: rbogdan@eti.pg.edu.pl (R. Bogdanowicz).

https://doi.org/10.1016/j.jiec.2023.07.043

Due to the asymmetric structure of FLBP, the index of refraction and extinction coefficient also depend on the polarization direction [33–35]. Research findings demonstrate that BP exhibits a lack of distinct features in the zig-zag direction [32,36]. However, owing to its unique structure, BP possesses significant anisotropy [10], which can be beneficial for optical and optoelectronic applications [29–31]. Next, *ab-initio* studies of black phosphorus (BP) reported attractive optical and electronic properties followed by extended experimental investigations [37]. The band structure of this material was estimated using Density Functional Theory (DFT) simulation utilizing supercell with a horizontal size equal to a single primitive cell [38], which was possible due to the symmetry of black phosphorus structures [39]. The DFT simulations allow for prediction of optical anisotropy of phosphorene electron and phonon band structure induced by applied strain [40,41].

However, it was discovered that BP flakes undergo degradation when exposed to the surrounding environment, with this effect being even more significant for single, larger flakes [42]. Therefore, the utmost importance lies in regulating and improving the stability of BP materials to effectively incorporate desired functionalities. One instance of this is the introduction of phosphorus doping in graphene, which not only enhances its bandgap but also enables the production of H_2 through photocatalysis [43]. Additionally, the implementation of a nanocomposite approach can be employed to fine-tune reduction processes [44,45] or customize the stability of optical parameters when exposed to UV irradiation [45]. It is important to emphasize that the utilization of multilayered complexes of BP flakes offers enhanced versatility for optical applications, resulting in higher wetting angles achieved through various surface termination methods [46]. By adjusting the number of layers and reducing the size of flakes in composite materials made of 2D materials, it becomes possible to enhance stability and fine-tune the optical properties [47].

The electrochemical exfoliation and surface modification techniques [48] have demonstrated high efficiency and precise control in shaping the geometry of flakes, enabling the exquisite fabrication of BP flakes [8]. The type of electrolyte used in the exfoliation process plays a crucial role in the formation of BP flakes. According to Kovalska *et al.* [49], employing anhydrous solvents such as DMF and acetonitrile in an oxygen-free environment prevents the oxidation of the resulting phosphorene, leading to enhanced stability and durability.

This paper presents the fabrication of a series of FLBP composite coatings through the fractionation of electrochemically exfoliated flakes using centrifugation at varying speeds. This novel approach enables the customization of the optical properties of the FLBP coatings by fractionating the flakes based on their sizes, which has not been previously reported. Moreover, the optical constants of the FLBP coatings were characterized through combined spectroscopic ellipsometry studies, DFT simulation supported by Raman spectroscopy, and polarization microscopy. The obtained results revealed optical constants similar to those of individual, isolated flakes. Detailed analysis was conducted on the dispersion of the refractive index, extinction coefficient, and thickness across a wide spectrum ranging from the near-infrared to the deep-ultraviolet, which is crucial for future optical applications.

Experimental techniques

Materials and fabrication

Black Phosphorous (BP, 99.998%) was obtained from Smart Elements, dimethyl sulfoxide (DMSO, ≥99.9%), and tetrabutylammonium tetrafluoroborate ($TBABF_4$, ≥99.0%) from Sigma Aldrich. All reagents were used without further purification. The purge gas (argon) was purchased from Air Liquide.

Black phosphorus crystal (24.5 mg) was electrochemically exfoliated like in a 0.01 M solution of tetrabutylammonium tetrafluoroborate ($TBABF_4$) in dimethyl sulfoxide (DMSO). The BP cathode and the platinum wire anode were separated by a fixed distance 1 cm. Exfoliation was carried out by applying a preliminary DC voltage of 2 V for 30 min, after which the voltage was increased to 4 V and maintained for 12 h. Afterward, the exfoliated material was sonicated into an ultrasound bath (Polsonic Sonic-3, 160 W, 40 kHz) for 3 minutes to disperse the FLBP in the solvent. The process of electrochemical exfoliation was performed in a stream of argon. Analogous strategy was successfully applied for exfoliation for separated BP flakes for i.e. electrochemical sensing [25,50], energy storage [8] or tuning optical polarization [51,52] (see more details in Table. 2.).

Here, the electrochemically exfoliated BP dispersed in DMSO at a concentration of 0.88 mg/ml was separated into the different fraction sizes by centrifugation. The resulting sample was successively centrifuged at different speeds of 9000, 6000 and 3000 rpm. The supernatant was collected after centrifugation at 9000 rpm, the FLBP residue was supplemented with DMSO and centrifuged again at 6000 rpm, another supernatant fraction was collected and the residue was supplemented with DMSO and centrifuged at 3000 rpm. The fractions obtained after centrifugation at 9000, 6000 and 3000 rpm were spotted onto silicon in an amount of 20 μL and evaporated at 60 °C under reduced pressure in a glovebox. The layers obtained from the supernatants after centrifugation at 9000 rpm, 6000 rpm and 3000 rpm are named FLBP-9, FLBP-6 and FLBP-3 respectively. The reference sample is the FLBP-0 sample obtained from uncentrifuged FLBP in DMSO suspension. FLBP-0 is a layer prepared by applying 20 μL on a silicon substrate and evaporating at 60 °C under reduced pressure in glovebox conditions from the fraction taken from the BP-DMSO suspension after preparation of FLBP by electrochemical exfoliation (no centrifugation).

Characterization methods

The FLBP samples were examined using a LAB 40 POL polarization microscope from OPTA-TECH, to obtain information about their structures and the polarization parameters. The microscope was working in reflection mode. Microscopy images were obtained when the polarizers were placed in parallel (vision view) and perpendicular relative to each other (polarization view). A Phenom XL scanning electron microscope (SEM) from Thermo Fisher Scientific was used to determine the surface topography with the operating voltage set at 15 kV. During the measurements, the backscatter electron detector and secondary electron detector were used.

The spectroscopic azimuths, Ψ and Δ, were measured using a V-VASE device from J.A. Woollam Co., Inc. for an angle of incidence of 70° in the NIR-vis-UV spectral range (193–2000 nm; 0.6–6.5 eV). The WVASE32 software (J.A. Woollam Co., Inc.) was used to perform the fit procedure.

The Raman spectra were recorded with an inVia confocal micro-Raman system (Renishaw), operating with a 1200 groves/mm grid. To ensure minimal destruction, the samples were excited by the 514 nm laser at a significantly reduced power, and at least five scans were recorded and averaged for each investigated surface point. Each sample was analyzed at five independent points. The lateral resolution on the sample surface was 5 μm at 50 × magnification.

To derive the theoretical optical constants of the few-layer black phosphorus structure, a series of DFT simulations was prepared. The model of the structure was made in QuantumATK based on the structure of black phosphorus [53]. Several copies of the

structure were prepared with different numbers of layers, which included the structure series from monolayer to eight layers, and the infinite-layer bulk structure, which represents the black phosphorus. Each finite-layer structure comprised two horizontal repetitions of the structure primitive cell. The lattice constants for the structure were approximately 3.32 Ang in the zigzag direction and 4.6 Ang in the armchair direction. The AB stacking was used since it leads to the most stable configuration [54].

The geometries of all of the structures were optimized before the optical spectrum calculations were performed using the Broyden-Fletcher-Goldfarb-Shanno (L-BFGS) algorithm with the stop criteria such that all forces have to be lower than 10^{-4} eV/Ang. The simulation was run using QuantumATK version Q-2019.12, Synopsys QuantumATK [55], using the *ab initio* DFT method with a linear combination of atomic orbitals (LCAO). The general gradient approximation (GGA) with PBE (Perdew-Burke-Ernzerhof) functionals were applied for the description of the electron density. The numerical parameters of each simulation were: 20x16x1 Monkhorst Pack k-point sampling and 300.0 Hartree mesh cut-off energy.

The material's response to the variable electromagnetic field was calculated using the Kubo-Greenwood formula [56]. The calculations were run for 4001 photon energy points in the range from 0.62 to 7 eV. The resulting susceptibility tensor was recalculated into refraction (n), reflection (R), extinction (κ) coefficient tensors. The formulas (1–4), similar to these proposed by [57], were used for this calculation.

$$\epsilon_r(\omega) = (1 + \chi(\omega)) \tag{1}$$

$$n = \sqrt{\frac{\sqrt{\epsilon_1^2 + \epsilon_2^2} + \epsilon_1}{2}} \tag{2}$$

$$\kappa = \sqrt{\frac{\sqrt{\epsilon_1^2 + \epsilon_2^2} - \epsilon_1}{2}} \tag{3}$$

$$R = \frac{(1-n)^2 + \kappa^2}{(1+n)^2 + \kappa^2} \tag{4}$$

Where χ is the susceptibility, ϵ_1 is the real part of the dielectric constant, and ϵ_2 is the imaginary part of the dielectric constant.

Results and discussion

Morphologic and polarization imaging of FLBP

To gather structural information about the FLBP samples, the polarization (see Fig. 1) and morphology SEM images were obtained (see Fig. 2). The FLBP coatings reveal a multi-flake morphology comprising flakes superimposed on each other. As displayed in the polarization microscopy, increasing the centrifugation speed fractioned the flake size. Each large flake induces local polarization anisotropy. The lower speeds resulted in a large amount of bigger flakes, causing microscale depolarization effects (see Fig. 1b).

The flake size and thickness heterogeneity impact the average polarization distribution of the FLBP coating. The morphology analysis conducted by SEM displays average flake sizes of 4.8 ± 5.6, 2.1 ± 2.0, 1.3 ± 0.52, 0.72 ± 0.75 μm for the as-exfoliated FLBP-0 FLBP-3, FLBP6, and FLBP-9, respectively. The FLBP-6 thickness was estimated by scanning electron microscopy. The thickness of 36 nm was achieved using average of 3 points at the cross-section. The lowest gradient of FLBP coating thickness variations was achieved for 6 k rpm, suggesting that this fraction is the largely dominating initial exfoliated FLBP slurry. FLBP-6 also shows the most equal polarization variations along with well-organized morphology (see Fig. 2c). Increasing the speed up to 9 k rpm results in local deposits of flake islands, resulting in non-continuous coverage. There are not enough of the smallest BP flakes in the FLBP-9 sample to fully cover the substrate (see Fig. 2d).

It should be mentioned that the observed image patterns also result from the edges of BP flakes, showing a shift in polarization anisotropy from values obtained for the interior of the flakes. This effect was attributed to the 1D confinement and reduced symmetry at the edges, modifying the electronic charge distribution [58]. The flakes in the FLBP coatings are misoriented. Thus, the polarization signal is averaged by the optical anisotropy, which for energies < 3 eV exhibits the variation of the absorption coefficient. It achieves approx. 2 orders of magnitude larger values for the polarization transmitted along the armchair (AC) direction than that propagated along the zigzag (ZZ) direction [59]. The optical anisotropy of the edges is mostly independent of folds, wrinkles, and oxides.

The set of FLPB samples with different centrifugation speeds was imaged with a polarization microscopy at three angles of 0°, 30°, and 60° (see Fig. 3). FLBP are characterized by optical anisotropy, hence its structure can be observed under crossed polarizers. The pattern of FLBP-0 and FLBP-3 (see Fig. 3 a,b) consist of multiple flakes forming an almost continuous layer. Different intensity of BP flakes reflectance in the polarization image indicate that they are randomly disoriented. In turn, FLBP-6 and FLPB-9 shows lower flakes density than FLBP-0 and FLBP-3 revealing in polarization images separated flakes scattered across the Si surfaces (see Fig. 3 c,d). Due to the interlayer coupling effect in BP, the optical absorption of polarized light is more intense along the AC direction [60]. As a result, reflected light polarized along the ZZ direction displays higher intensities.

For this reason, a rotated FLBP sample analyzed with steady-state light periodically changes its reflectance [61]. The obvious changes in the intensity of reflectance of separated BP flake in a function of the rotation angle are shown in Fig. 3. Hence, the FLBP layers are characterized by birefringence being in agreement with previous works [58,62]. The analysis of the patterns of the polarization images of BP flakes presents a shift in polarization anisotropy originated mainly from the central region of the flake. Furthermore, the BP flake is dark when the polarization of the incident light is oriented along the FLBP crystal axis. The rotation of the sample causes the increase of phase retardance and, hence, the polarization of the incident light changes after reflection from FLBP flake. Moreover, the individual flakes also differ in colour due to the polarization disturbances, which are attributed to local defects (i.e. thickness inhomogeneities, fractures, folding etc.).

According to microscopic studies, the deposited FLBP layers are heterogenous and consists of multiple flakes disoriented and locally overlapped. Importantly, the Raman spectra collected during the experiment should be attributed to the few-layer phosphorene. These facts suggest that our layer is composed of multiple few-layer phosphorene flakes, which are randomly oriented. The separated flakes reveal typical birefringence in polarization microscopy, while we focused our study on the integrated optical constants of composite coating of FLBP. Spectroscopic ellipsometry utilizes ellipsoidal spot size (3 mm wide and 10 mm long) being considerably larger than the size of the flake. Thus, we could assume that we measure the signal from multiple flakes at once, which has been superposition of responses originating from light interaction with dielectric constants of all the orientations of a single flake. Each flake is optically anisotropic (biaxial); however, because of the random orientation of the flakes, the measured

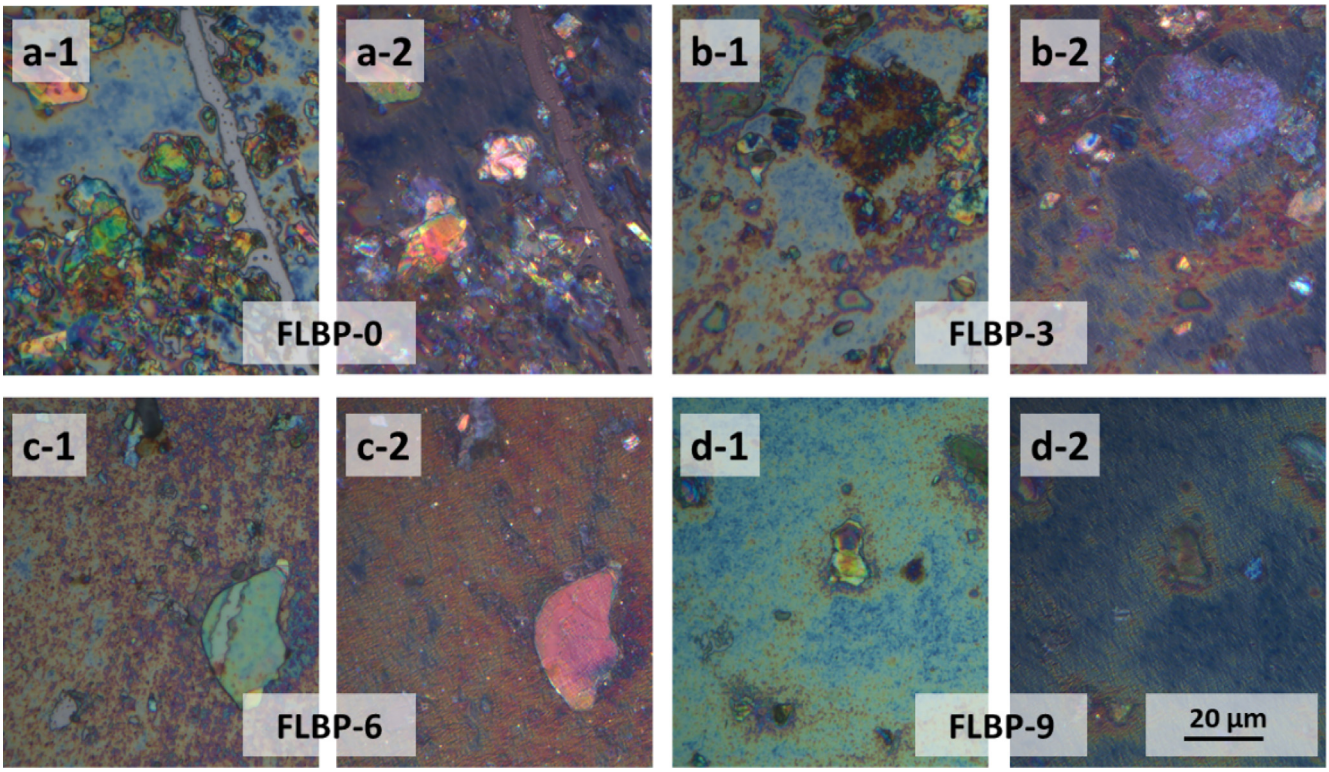

Fig. 1. Polarization microscopy images of FLBP samples fabricated with different centrifuged speeds: a – 0 rpm, b – 3000 rpm, c – 6000 rpm, d – 9000 rpm. 1 – vision view; 2 – crossed polarizer view.

effective optical constant stands semi-isotropic. The concept is analogous to this typically applied during the theoretical analysis of the properties of composite materials.

Fig. 4 shows the Raman spectra of the BP with different centrifugation speeds. We observed 3 modes centered at 362.5 cm^{-1}, 439.3 cm^{-1}, and 467.6 cm^{-1} assigned to A_{g1}, B_{2g} and A_{g2}, respectively [63]. The Si band centered at 520 cm^{-1} corresponds to the silicon substrate. In multilayered BP clusters, due to van der Waals interactions between the layers, the oscillations of P atoms are damped and a redshift of the vibration can be observed [64–66].

The observed characteristic Raman bands indicate a multilayered structure of the obtained FLBP flakes. The average shifts of the bands are summarized in Fig. 4b and Table 1. The positions of the bands vary only slightly as a function of the centrifugation speed. The shift in the position of the bands toward a lower wavenumber was observed. The higher speeds of centrifugation resulted in an amplified redshift of bands in Raman spectra, indicating a greater presence of FLBP flakes in the samples. Castellanos-Gomez *et al.* [67] also reported similar observations when studying mechanically exfoliated BP flakes. From the presented results, it can be concluded that the centrifugation of a suspension of phosphorus flakes of assorted sizes and number of layers leads to segregation of the flakes in terms of mass and not the number of layers. Samples centrifuged at higher speeds have a higher content of smaller but still multilayer phosphorus flakes.

Complex index of refraction for few-layer and bulk BP

The spectroscopic ellipsometry data measured on the FLBP samples with different centrifuged speeds are shown in Fig. 5. The measurement range was 260–830 nm. It can be assumed that the FLBP coating comprises many flakes superimposed on each other. The different centrifugation speeds and drop-cast deposition methods also affect the thickness of the samples. All this contributes to the apparent difference between the ellipsometric spectra. The *Delta* angle shows an increase in value for higher centrifugation speeds, which is attributed to the thinning of the deposited coating. In contrast, the *Psi* azimuths of FLBP coating show minor variations, proving the homogeneous composition of the stacked BP flakes.

The FLBP-6 characteristics were used in the further analyses. First, ellipsometric measurements were repeated in a wider range: 190–2000 nm. The obtained data is shown in Fig. 6. The five medium optical model (from bottom to top: Si\native SiO_2\BP layer\-surface roughness\ambient) was used to determine optical properties and thickness of the BP films. The complex refractive index of substate (both Si and SiO_2) were taken from the database of optical constants [68]. The optical constants of the BP thin film were parameterized using a set of oscillators. The surface roughness was modeled using a Bruggeman Effective Medium Approximation (BEMA) approach [68,69]. The standard MSE was estimated to be 10.

The optical constants of the BP layer were determined as effective quantities, which includes all non-idealities of the synthesized material. This approach can be justified taking into account, that the diameter of the incident light beam was about 3 mm, however, for the chosen angle of incidence (70 deg.) the shape of the spot is ellipsoidal (about 3 mm wide and 10 mm long). As a result of the analysis, the thickness of the BP layer was determined to be 38.4 nm. Information on the refractive index (see Fig. 7a) and extinction coefficient (see Fig. 7b) were also obtained. Looking at Fig. 7a, we can see that the refractive index for FLBP-6 increases rapidly, reaching peak of 3.5 at 300 nm, 3.8 at 338 nm, and the highest value 5.1 at 384 nm. After that, it steadily decreases. A similar tendency has been shown in previous work [70].

The high coefficient of extinction below 400 nm indicates the high absorption of BP in this range (see Fig. 7b) [71], which is in agreement with previous works [33,72,73]. For wavelengths above

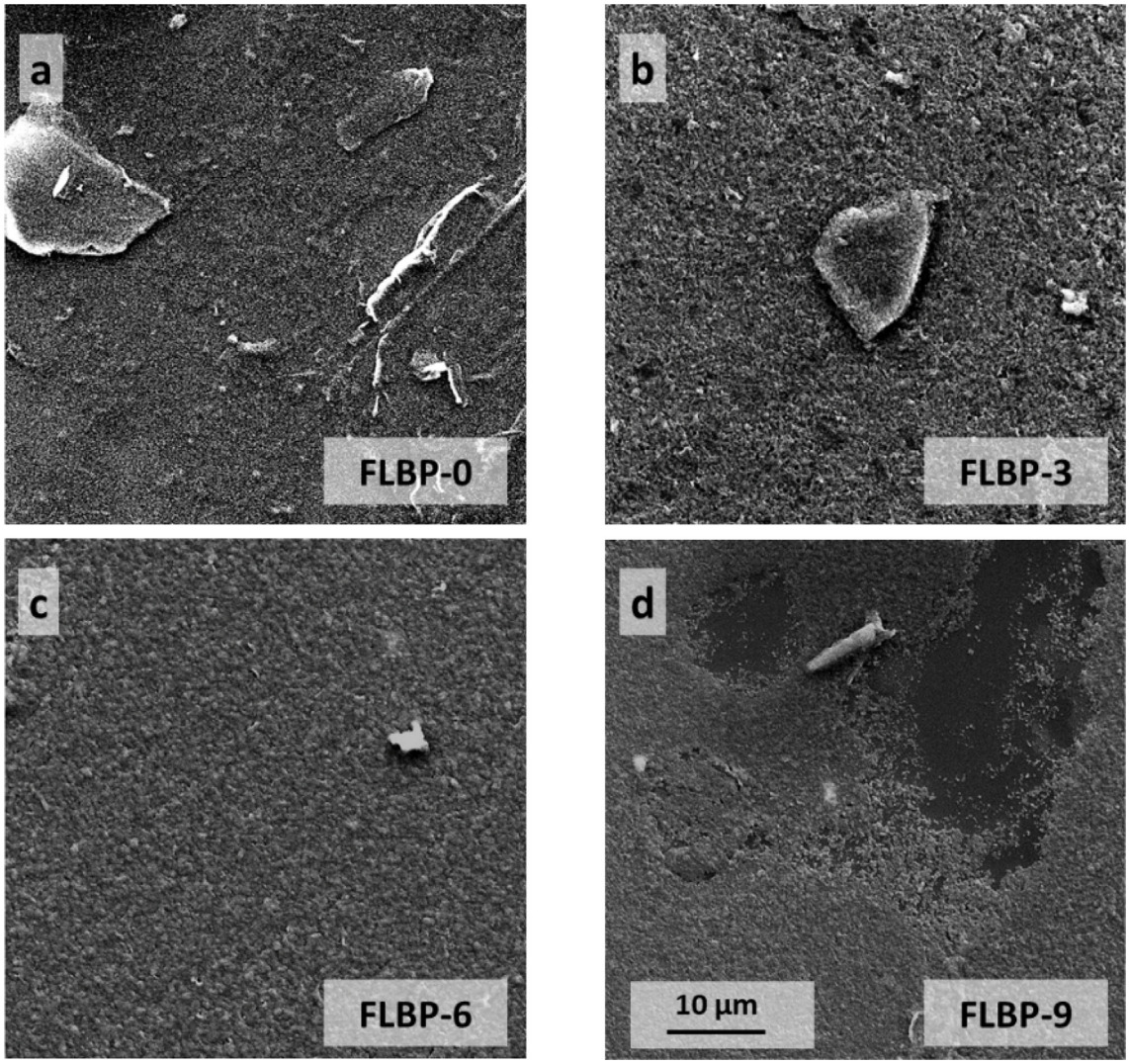

Fig. 2. SEM images of FLBP samples fabricated with different centrifuge speeds (drop-casted on Si substrate): a – 0 rpm, b – 3000 rpm, c – 6000 rpm, and d – 9000 rpm.

400 nm, the coefficient drops, which indicates that the material becomes transparent in this range. Three peaks are seen in Fig. 6b – at 226 nm, 290 nm, and 360 nm. Guo *et al.* reported absorption peaks at 310 nm, 380 nm, and 470 nm for phosphorene in NMP [64].

DFT simulation of anisotropic optical constants of few-layer BP

The optical properties of an anisotropic material such as phosphorene are described by tensors. This tensor determines the response of the material depending on the direction of the external electric field. In the case presented in the article, we decided to only analyze the diagonal components of the dielectric constant tensor. The coordinate system used during the calculation was oriented such that all three axes were coincidental with the principal directions of the phosphorene crystal lattice. The X-axis was pointing in the zigzag direction, the Z-axis was pointing in the armchair direction, and finally, the Y-axis was pointing in the interlayer direction, completing the right-handed coordinate system.

The experimental and simulated results are compared in Fig. 8. As was revealed in the DFT calculation, the values of the refractive index and the extinction coefficient depend on the crystal orientation and the thickness. Both parameters increase when the number of layers increases. Some theoretical studies also show that phosphorene optical properties can be affected by edge effects both in the case of nanoribbons [74,75] and nanodots [76]. However, the effect is significant only if the width of the structure is close to 1 nm and decays rapidly with the growth of structure size.

The size of flakes in our experiments is ~1 µm. That is, all edge effects can be safely neglected. The DFT simulation for 6-layer FLBP corresponds superlatively to the experimental results (see Fig. 8c). In addition, the simulated extinction coefficients in the zigzag (XX) and armchair (ZZ) directions are characterized by two peaks that are also visible in the experimental results.

However, as was mentioned earlier, the orientations of the flakes in the sample are arbitrary. Since the spot size during measurements is significantly larger than the single flake size, the average optical constant of multiple flakes is measured. The multiple randomly oriented flakes have their input to measured response. As a result, the measured optical constant is isotropic. However optical constant of each individual flake is strongly anisotropic. The DFT calculations refer to the single FLBP flake, so the calculated response is tensor which has three principal components XX, YY and ZZ. The peaks in an extinction coefficient of FLBP are located at 4.05 eV and 4.12 eV, which are related to inter-band transitions between the valence and conduction bands [77] determined by DFT. The presented results are consistent with that reported for the dielectric constant [73]. The behavior of the optical constants

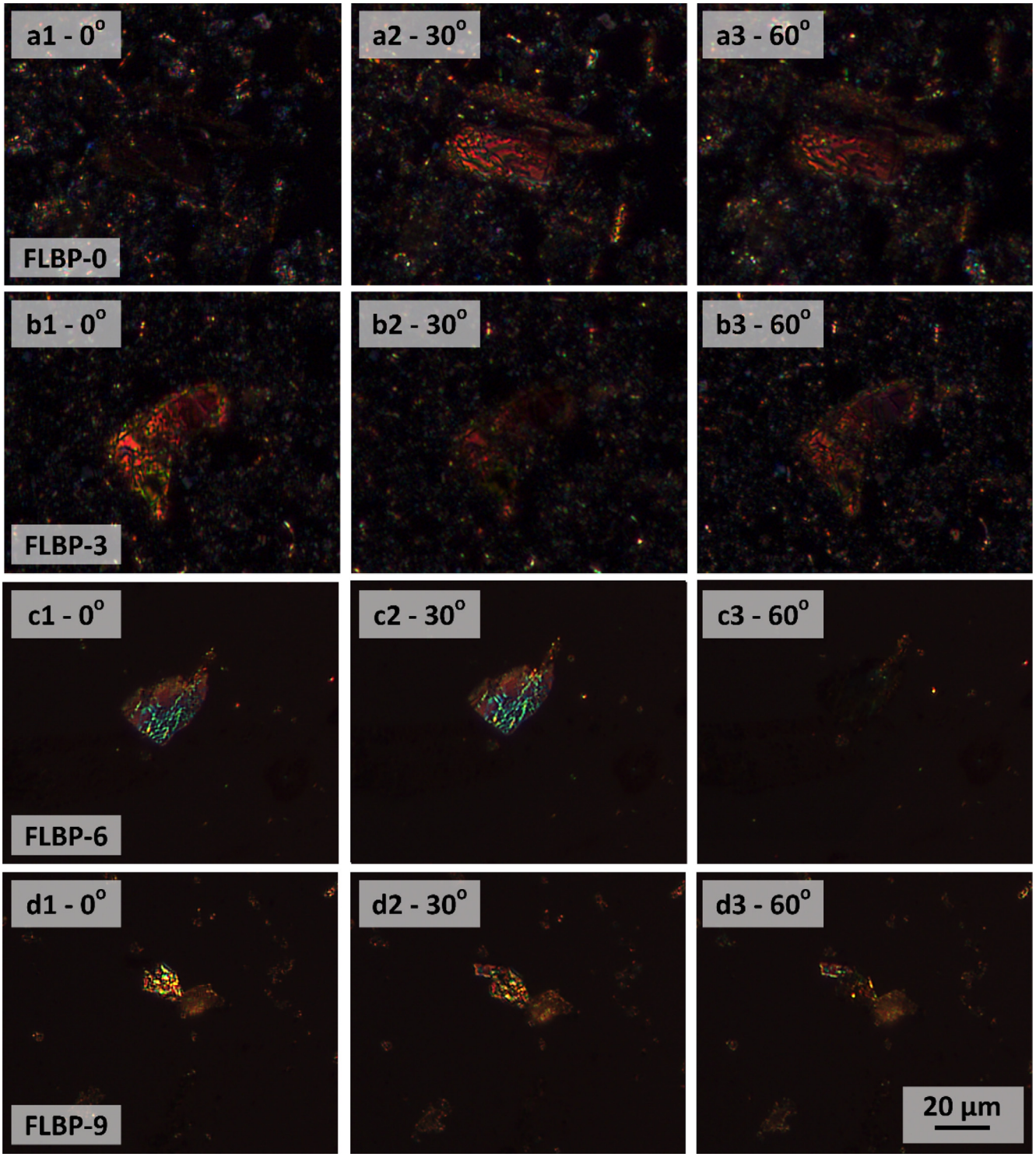

Fig. 3. Polarization microscopy images of FLBP samples fabricated with different centrifuged speeds: ax – 0 rpm, bx – 3000 rpm, cx – 6000 rpm, dx – 9000 rpm with 1 – 0°, 2 –30° and 3- 60° rotational angle.

in the energy range of 1–7 eV relates strictly to the FLBP band structure, indicating relatively high absorption. It is caused mainly by electronic transitions from the valance to the conduction band.

The smooth threshold of the absorption could be observed at approx. 2 eV in dispersion curves. The optical band gap of 3.1 eV was estimated from the Tauc plot [(αhυ)2 vs hυ curve] utilizing nk data of FLBP-6 achieved from spectroscopic ellipsometry. Comparable values were reported previously for few-layer flakes of BP fabricated by the high speed centrifugation of liquid phase exfoliated suspensions [78–80]. The higher value of optical band gap than estimated for bulk or single flakes [81] was assigned to the reduction of the average thickness of BP flakes thanks to the separation induced by centrifugation. The optical band gap is attributed to the high-energy band-to-band transition while the theoretically predicted values are commonly assigned to the low-energy band-to-band transition. Furthermore, Woomer et al. [82] claimed that

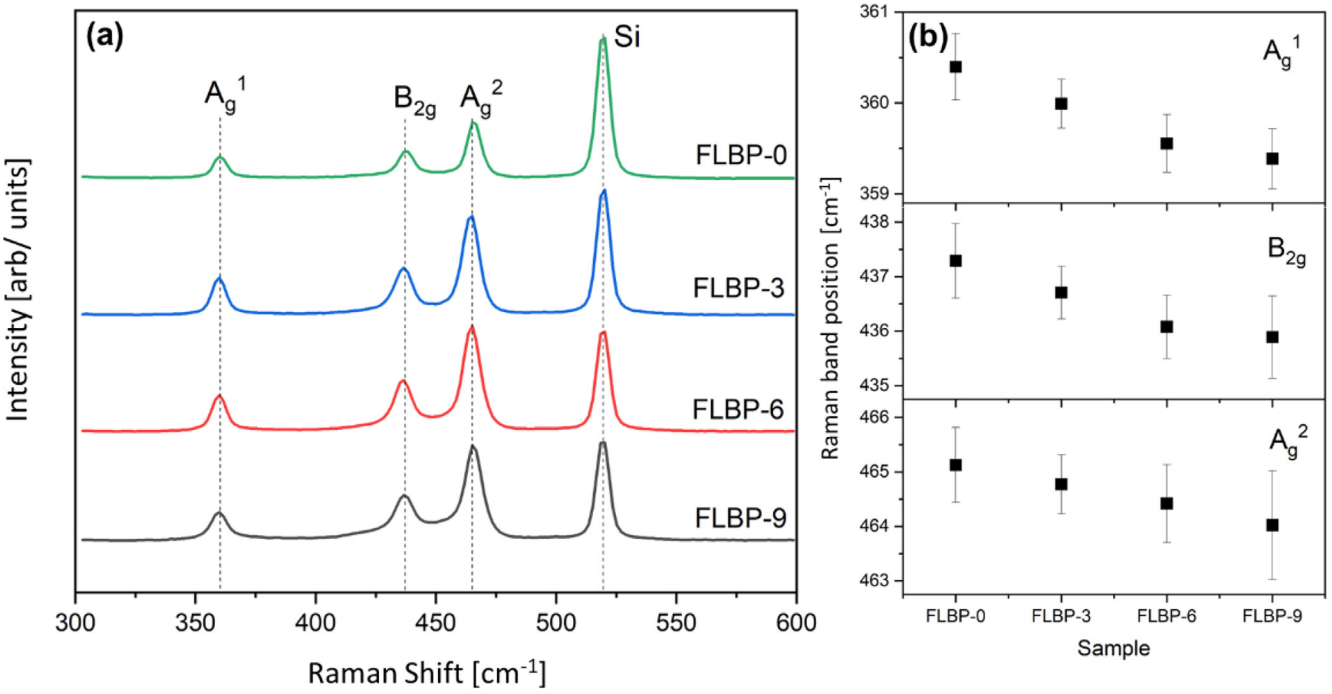

Fig. 4. Raman spectra of FLBP samples (a); A_g^1, B_{2g}, and A_g^2 average band positions (b) estimated for samples centrifuged at different speeds.

Table 1
Position of Raman bands estimated for FLBP samples centrifuged at different speeds.

ID	A_g^1	SD (A_g^1)	B_{2g}	SD (B_{2g})	A_g^2	SD (A_g^2)
FLBP-0	360.40	0.37	437.29	0.68	465.13	0.69
FLBP-3	359.99	0.27	436.71	0.48	464.77	0.54
FLBP-6	359.56	0.32	436.08	0.58	464.42	0.71
FLBP-9	359.39	0.33	435.89	0.76	464.02	1.00

Table 2
Comparison of optical parameters of FLBP, achieved for various fabrication techniques.

Synthesis exfoliation method	Samples Topography	Refractive index	Reference
Mechanical exfoliation	Single flake (thickness- 176–496 nm, size-100 μm)	4.0 (540 nm)	[70]
Mechanical exfoliation	Single flake (thickness- 14–30 nm, size- 25 μm)	3.56-zig zag direction; 3.29- armchair direction (532 nm)	[83]
Mechanical exfoliation	Single flake (thickness- 5 nm, size- 15 μm)	3.0 -zig zag direction; 2.9- armchair direction (532 nm)	[35]
Computational method DFT	Single flake -super-cell	2.76 -zig zag direction; 2.72 armchair direction (532 nm)	[19]
Computational method DFT	Single flake -super-cell	3.65 -zig zag direction; 3.36 armchair direction (532 nm)	[84]
Computational method DFT	BP nanotubes	2.7 -zig zag direction; 2.3- armchair direction (532 nm)	[85]
Electrochemical exfoliation	few-layer black phosphorus	3.8 (532 nm)	This work

Tauc analysis would fail in bandgap estimation in BP flakes suspensions (i.e. light scattering, anisotropy, variation in band gap). Obviously, centrifugation process induces various defects as flakes coiling, folding and fracturing affecting band gap value. It could be specified here as an absorption edge attributed to the transition from the highest valance to the lowest conduction band.

Only a limited number of authors have previously investigated the optical constants of phosphorene flakes, focusing on deriving the refractive index and extinction coefficient dispersions of BP within the visible and near-infrared range (refer to Table 2). These measurements were accomplished through transmittance analysis [70] or the examination of anisotropic optical contrast spectra, followed by the application of the Fresnel equation [83]. Moreover, Schuster et al. [86] conducted a Kramers-Kronig analysis (KKA) to estimate the dispersion of dielectric constants. This analysis was based on electron energy loss spectroscopy (EELS) spectra obtained through transmission mode measurements of mechanically exfoliated single flake black phosphorus (BP).Next, Asahina et al. [84] and Qiao et al. [19] employed self-consistent pseudopotential calculations to compute the frequency-dependent dielectric function of black phosphorus, utilizing the band structure and wavefunctions as fundamental inputs.

It should be added that classical optical modeling of optical constants using ellipsometric data considers the standard interference effects induced by multiple reflections in the FLBP flake and substrate interfaces. Islam *et al.* [87] showed that the classical model should be corrected by considering different optical constants along the AC and ZZ directions. Thus, the optical constants simu-

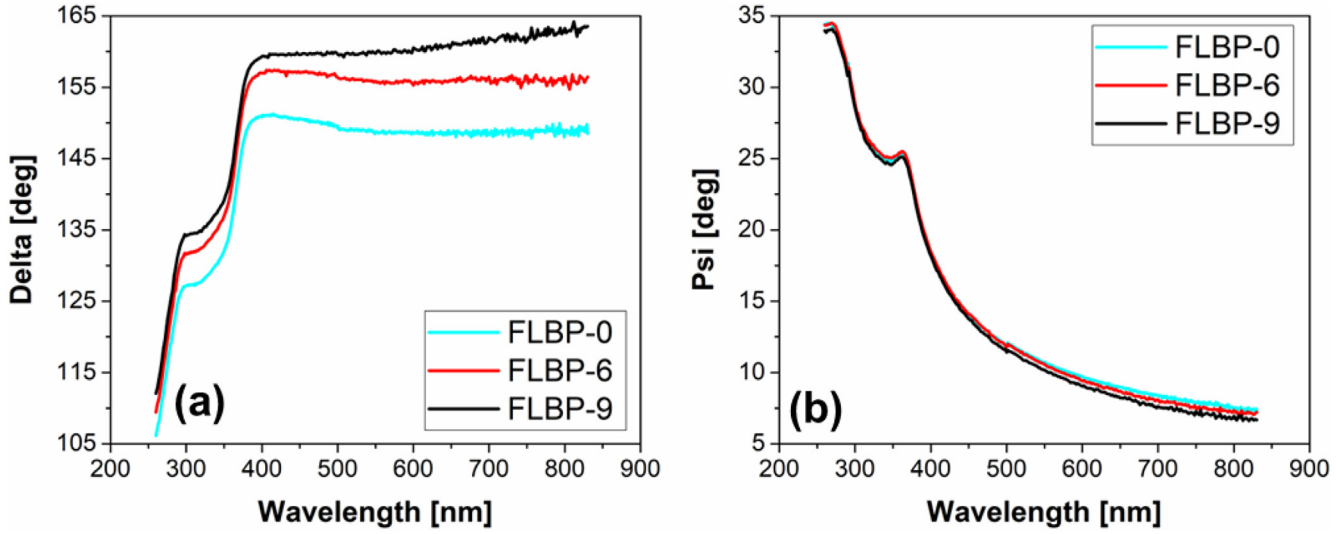

Fig. 5. Variations of ellipsometric, experimental data of (a) Delta and (b) Psi azimuths recorded for FLBP samples with different centrifuge speeds.

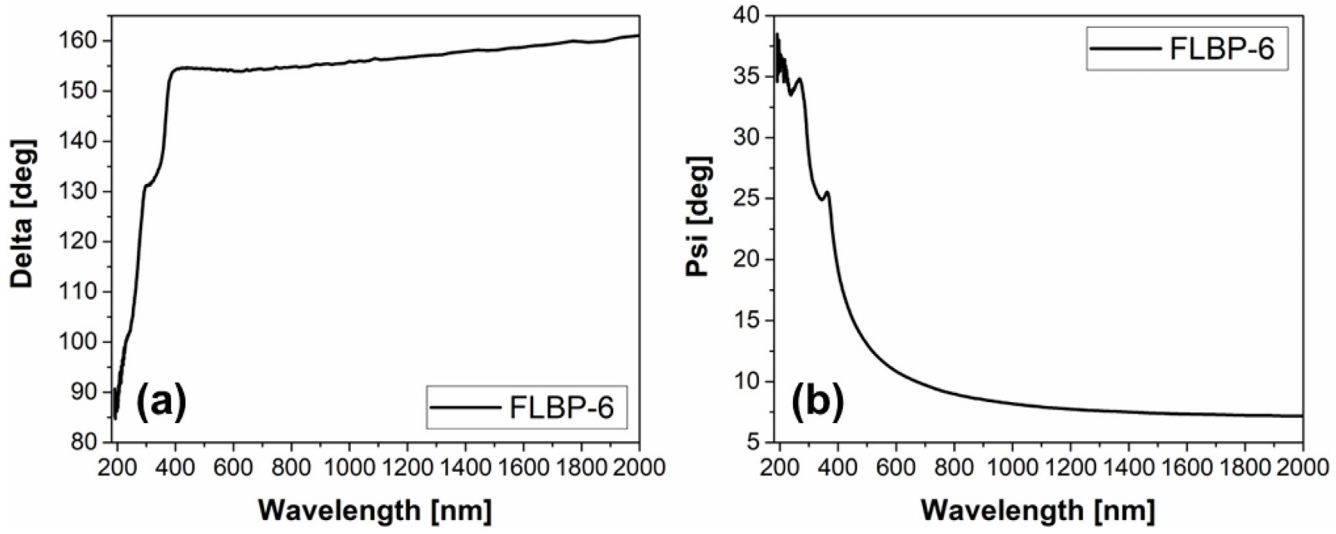

Fig. 6. Wide wavelength range variation of ellipsometric angles of (a) Delta and (b) Psi of FLBP-6 sample centrifuged at 6000 rpm recorded by the spectroscopic ellipsometry.

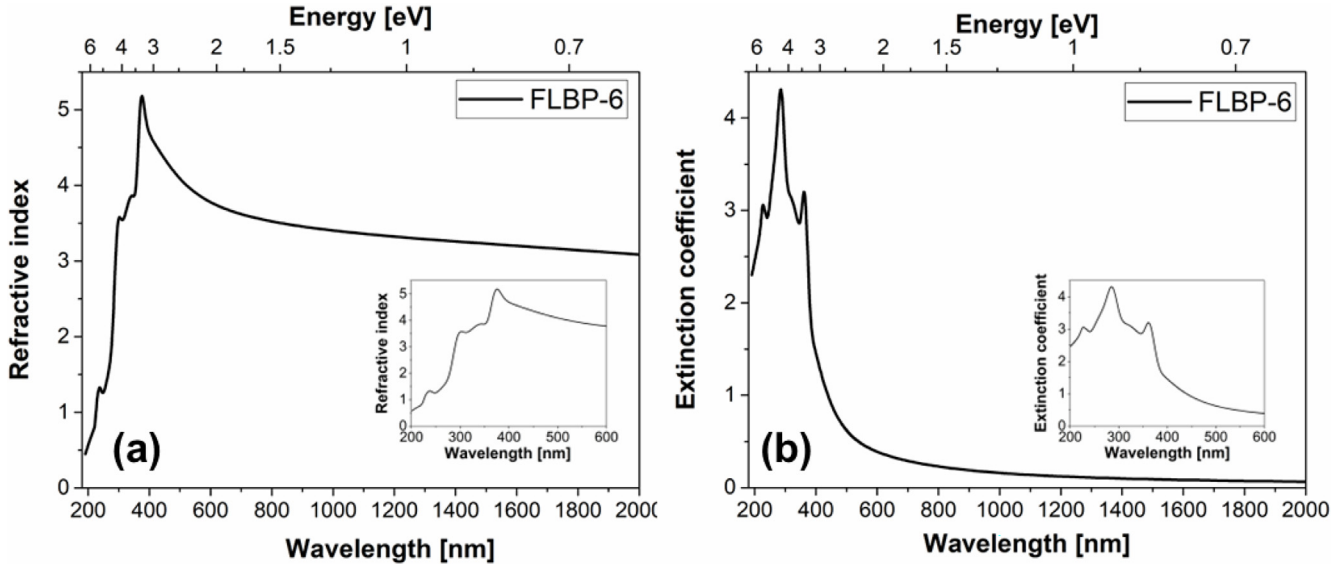

Fig. 7. Optical constants: (a) – refractive index and (b) – extinction coefficient of FLBP-6 sample centrifuged at 6000 rpm derived from spectroscopic ellipsometry.

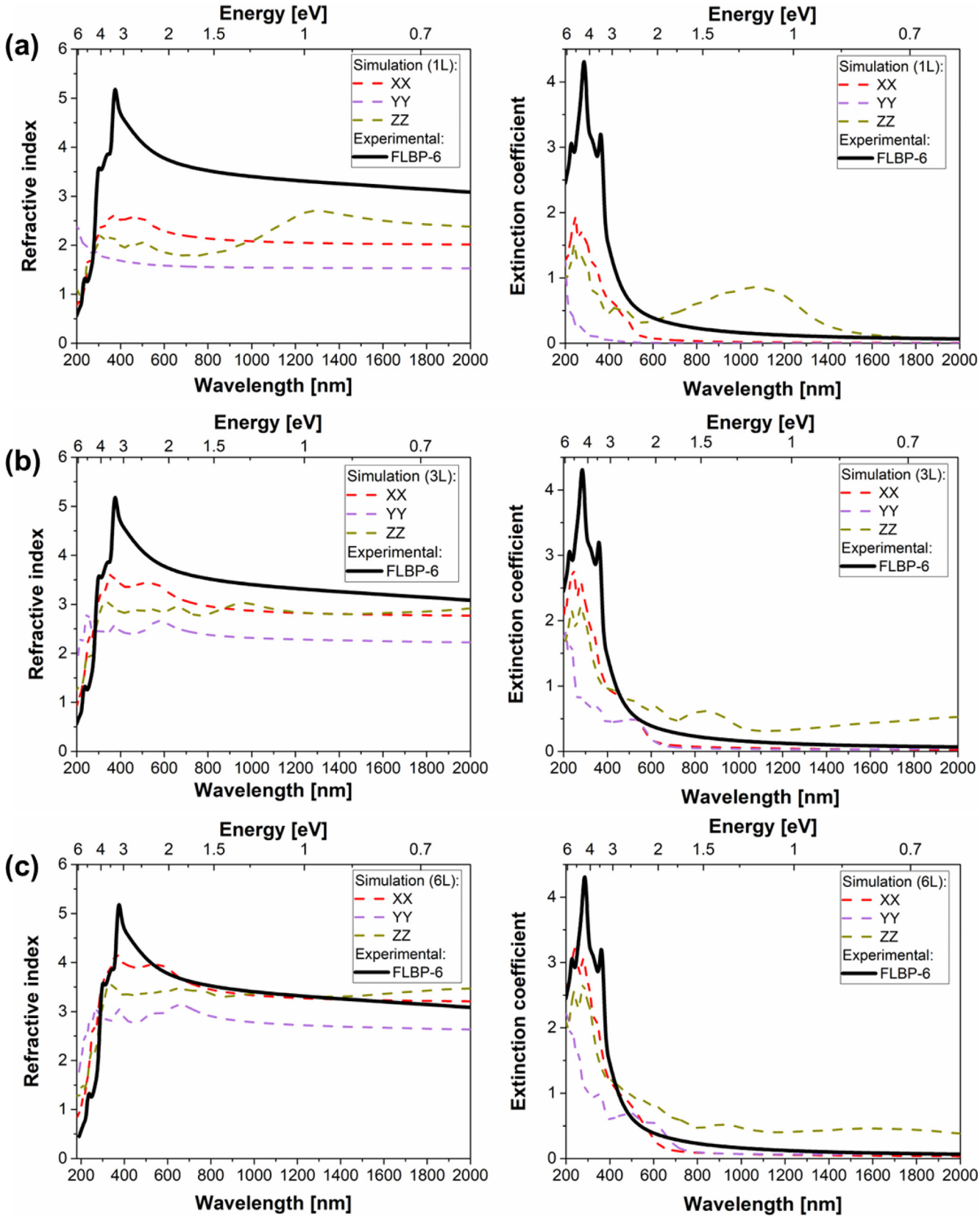

Fig. 8. Comparison of refractive index and extinction coefficient achieved from experimental and DFT simulation results. DFT calculations were performed for (a) – single-layer (1L), (b) – three-layer (3L), and (c) – six-layer (6L) FLBP.

lated ab initio by DFT reveal a more precise estimation that fits the optical anisotropy of the BP flakes. Next, Mao et al. reported [35] that analysis of RGB-separated microscopic images in the function of rotation angle could be applied to determine BP directions orientations. A simplified image analysis does not consider optical anisotropy, which, therefore, depending on the thickness of the

flakes, causes contradictory findings in crystal orientation analyses [88]. Furthermore, Islam *et al.* [87] showed polarization-corrected reflectance data that revealed the crystal orientation matching the experimental data independently of the substrate type or FLBP thickness.

The low energy peak localized at *ca.* 2.4 eV could be attributed to intra-layer excitons at low energies or blue-shifted excitons that appear due to inter-layer effect, similar to quantum wells [32]. This effect causes major in-plane anisotropy, inducing a band with much higher effective electron transport along the AC direction than in the ZZ direction.

The anisotropic absorption properties suggest that the extinction coefficient of BP flakes defines and limits the applications of BP in photonics, waveguides, and directional optoelectronic devices. The specific edge optical absorption could be applied for selective excitation of nanoscale BP, tailoring the longitudinal distribution of excited charge carriers [58].

Conclusions

In summary, we obtained the complex optical constant of FLBP flake coatings forming large complexes, and compared them with 1–6 L BP by using the SE, classical optical modeling, and DFT simulations in the energy region of 1–6 eV. The dispersion of the complex optical constants of 2D FLBP gradually decreases with the decreasing L, which could be attributed to the tuned band gap of BP. A complex model of flake coatings that considers optical anisotropy flakes should be applied to extract the refractive index. We demonstrated that the reported BP excitonic peaks correspond to the bands achieved in the extinction coefficient k. The refractive index of the FLBP centrifugated at 6000 rpm layer exhibited a rapid increase, peaking at 3.5 at 300 nm, 3.8 at 338 nm, and reaching the highest value of 5.1 at 384 nm, followed by a gradual decrease. This trend aligns with previous experimental and simulation studies conducted on bulk BP or single BP flakes. The significant extinction coefficient below 400 nm indicates the strong absorption of BP within this range, while above 400 nm, the coefficient decreases, indicating the material's transparency. Notably, the dispersion curves exhibit a smooth threshold of absorption at approximately 2 eV. The optical band gap, estimated from the Tauc plot utilizing the nk data of FLBP obtained from spectroscopic ellipsometry, is determined to be 3.1 eV. Estimation of the optical constants of FLBP coatings has become more important since large, continuous BP films have not been achieved to date, which strongly limits their optical application. These findings provide valuable insights into the optical properties of FLBP and have implications for its potential applications in various fields.

Thus, it can be assumed that we have studied the optical signal originating from multiple flakes simultaneously, which is a superposition of responses originating from the interaction of light with the dielectric constants of differently oriented individual flakes. Each flake is optically anisotropic (biaxial); however, because of the random orientation of the flakes, the measured effective optical constant represents a kind of quasi-isotropic texture.

This concept is analogous to that typically used in the theoretical analysis of composite material properties. We state that such a complexes could be utilized as useful elements of new optical devices, such as photonic crystals and distributed Bragg reflectors or plasmonic nanostructures, due to their polarization and optical properties.

Declaration of Competing Interest

The authors declare that they have no known competing financial interests or personal relationships that could have appeared to influence the work reported in this paper.

Acknowledgments

This work was supported by the Polish National Science Centre [2016/22/E/ST7/00102] and financed from the budget funds for science for the years 2019/2023 as a research project in the "Diamond Grant" program framework No. 0063/DIA/2019/48.

References

[1] A.K. Singh, P. Kumar, D.J. Late, A. Kumar, S. Patel, J. Singh, Appl. Mater. Today (2018) 242–270, https://doi.org/10.1016/j.apmt.2018.09.003.
[2] K. Zhang, Y. Feng, F. Wang, Z. Yang, J. Wang, J. Mater. Chem. C (2017) 11992–12022, https://doi.org/10.1039/c7tc04300g.
[3] B.V.S. Reddy, K. Srinivas, N.S. Kumar, S. Ramesh, K.C.B. Naidu, P. Banerjee, R. Pothu, R. Boddula, Layered 2D Advanced Materials and Their Allied Applications, John Wiley & Sons Ltd, 2020, pp. 131–140.
[4] R. Mas-Ballesté, C. Gómez-Navarro, J. Gómez-Herrero, F. Zamora, Nanoscale (2011) 20–30, https://doi.org/10.1039/c0nr00323a.
[5] J. Zhao, H. Liu, Z. Yu, R. Quhe, S. Zhou, Y. Wang, C.C. Liu, H. Zhong, N. Han, J. Lu, Y. Yao, K. Wu, Prog. Mater Sci. (2016) 24–151, https://doi.org/10.1016/j.pmatsci.2016.04.001.
[6] M.E. Dávila, G. Le Lay, Sci. Rep. 6 (2016), https://doi.org/10.1038/srep20714.
[7] K. Cho, J. Yang, Y. Lu, J. Mater. Res. 32 (15) (2017) 2839–2847, https://doi.org/10.1557/jmr.2017.71.
[8] C. Shu, P.D.J. Zhou, P.D.Z. Jia, H. Zhang, Z. Liu, W. Tang, X. Sun, Chemistry – A European Journal 28 (49) (2022) e202200857.
[9] A. Chhetry, S. Sharma, S.C. Barman, H. Yoon, S. Ko, C. Park, S. Yoon, H. Kim, J.Y. Park, Adv. Funct. Mater. 31 (10) (2021) 2007661, https://doi.org/10.1002/adfm.202007661.
[10] G. Zhang, S. Huang, F. Wang, H. Yan, Laser Photonics Rev. 15 (6) (2021) 2000399, https://doi.org/10.1002/lpor.202000399.
[11] H.Y. Jun, S.O. Ryu, S.H. Kim, J.Y. Kim, C.-H. Chang, S.O. Ryu, C.-H. Choi, Adv. Electron. Mater. 7 (10) (2021) 2100577, https://doi.org/10.1002/aelm.202100577.
[12] F. Xia, H. Wang, Y. Jia, Nat Commun 5 (1) (2014) 4458, https://doi.org/10.1038/ncomms5458.
[13] S.C. Dhanabalan, J.S. Ponraj, Z. Guo, S. Li, Q. Bao, H. Zhang, Adv. Sci. (2017), https://doi.org/10.1002/advs.201600305.
[14] L. Liang, J. Wang, W. Lin, B.G. Sumpter, V. Meunier, M. Pan, Nano Lett. 14 (11) (2014) 6400–6406, https://doi.org/10.1021/nl502892t.
[15] H. Liu, A.T. Neal, Z. Zhu, Z. Luo, X. Xu, D. Tománek, P.D. Ye, ACS Nano 8 (4) (2014) 4033–4041, https://doi.org/10.1021/nn501226z.
[16] L. Li, Y. Yu, G.J. Ye, Q. Ge, X. Ou, H. Wu, D. Feng, X.H. Chen, Y. Zhang, Nat. Nanotechnol. 9 (5) (2014) 372–377, https://doi.org/10.1038/nnano.2014.35.
[17] A. Carvalho, M. Wang, X. Zhu, A.S. Rodin, H. Su, A.H. Castro Neto, Nat. Rev. Mater. 1 (11) (2016), https://doi.org/10.1038/natrevmats.2016.61.
[18] C. Zhao, M.C. Sekhar, W. Lu, C. Zhang, J. Lai, S. Jia, D. Sun, Nanotechnology 29 (24) (2018), https://doi.org/10.1088/1361-6528/aab98e.
[19] J. Qiao, X. Kong, Z.-X. Hu, F. Yang, W. Ji, Nat Commun 5 (1) (2014) 4475, https://doi.org/10.1038/ncomms5475.
[20] Z. Sofer, D. Sedmidubský, Š. Huber, J. Luxa, D. Bouša, C. Boothroyd, M. Pumera, Angewandte Chemie - International Edition 55 (10) (2016) 3382–3386, https://doi.org/10.1002/anie.201511309.
[21] N. Sultana, A. Degg, S. Upadhyaya, T. Nilges, N.S. Sarma, Materials Advances 3 (14) (2022) 5557–5574, https://doi.org/10.1039/D1MA01101D.
[22] A. Kumar, L. Viscardi, E. Faella, F. Giubileo, K. Intonti, A. Pelella, S. Sleziona, O. Kharsah, M. Schleberger, A. Di Bartolomeo, J Mater Sci 58 (6) (2023) 2689–2699, https://doi.org/10.1007/s10853-023-08169-0.
[23] C. Liu, L. Wang, X. Chen, J. Zhou, W. Tang, W. Guo, J. Wang, W. Lu, Nanoscale 10 (13) (2018) 5852–5858, https://doi.org/10.1039/c7nr09545g.
[24] A. Islam, A. van den Akker, P.X.-L. Feng, Opt. Mater. Express, OME 9(2) (2019) 526–35. 10.1364/OME.9.000526.
[25] Y. Zhang, Q. Jiang, P. Lang, N. Yuan, J. Tang, J. Alloy. Compd. 850 (2021), https://doi.org/10.1016/j.jallcom.2020.156580.
[26] Q.H. Wang, K. Kalantar-Zadeh, A. Kis, J.N. Coleman, M.S. Strano, Nat. Nanotechnol. 7 (11) (2012) 699–712, https://doi.org/10.1038/nnano.2012.193.
[27] S. Lan, S. Rodrigues, L. Kang, W. Cai, ACS Photonics 3 (7) (2016) 1176–1181, https://doi.org/10.1021/acsphotonics.6b00320.
[28] H.L. Liu, C.C. Shen, S.H. Su, C.L. Hsu, M.Y. Li, L.J. Li, Appl. Phys. Lett. 105 (20) (2014), https://doi.org/10.1063/1.4901836.
[29] W. Shen, C. Hu, S. Huo, Z. Sun, S. Fan, J. Liu, X. Hu, Opt. Lett. 43 (6) (2018) 1255, https://doi.org/10.1364/ol.43.001255.
[30] A. Castellanos-Gomez, J. Quereda, H.P. Van Der Meulen, N. Agraït, G. Rubio-Bollinger, Nanotechnology 27 (11) (2016), https://doi.org/10.1088/0957-4484/27/11/115705.
[31] G. Zhang, S. Huang, F. Wang, Q. Xing, C. Song, C. Wang, Y. Lei, M. Huang, H. Yan, Nat. Commun. 11 (1) (2020) 1–7, https://doi.org/10.1038/s41467-020-15699-7.
[32] A.M. Ross, G.M. Paternò, S. Dal Conte, F. Scotognella, E. Cinquanta, Materials 13 (24) (2020) 1–12, https://doi.org/10.3390/ma13245736.
[33] V. Musle, S. Choudhary, Opt. Quant. Electron. 50 (7) (2018) 285, https://doi.org/10.1007/s11082-018-1548-3.

[34] X. Wang, S. Lan, Adv. Opt. Photon. 8 (4) (2016) 618, https://doi.org/10.1364/aop.8.000618.
[35] N. Mao, J. Tang, L. Xie, J. Wu, B. Han, J. Lin, S. Deng, W. Ji, H. Xu, K. Liu, L. Tong, J. Zhang, J. Am. Chem. Soc. 138 (1) (2016) 300–305, https://doi.org/10.1021/jacs.5b10685.
[36] M.C. Sherrott, W.S. Whitney, D. Jariwala, S. Biswas, C.M. Went, J. Wong, G.R. Rossman, H.A. Atwater, Nano Lett. 19 (1) (2019) 269–276, https://doi.org/10.1021/acs.nanolett.8b03876.
[37] Y. Jing, X. Zhang, Z. Zhou, Wiley Interdiscip. Rev.: Comput. Mol. Sci. 6 (1) (2016) 5–19, https://doi.org/10.1002/wcms.1234.
[38] R. Fei, L. Yang, Nano Lett. 14 (5) (2014) 2884–2889, https://doi.org/10.1021/nl500935z.
[39] A. Chaves, W. Ji, J. Maassen, T. Dumitrică, T. Low, 2D Materials: Properties and Devices, 2017, pp. 381–412.
[40] M. Elahi, K. Khaliji, S.M. Tabatabaei, M. Pourfath, R. Asgari, Physical Review B - Condensed Matter and Materials Physics 91 (11) (2015), https://doi.org/10.1103/PhysRevB.91.115412.
[41] K. Pyrchla, R. Bogdanowicz, Appl. Surf. Sci. 528 (2020), https://doi.org/10.1016/j.apsusc.2020.147033.
[42] W. Shen, Z. Sun, S. Huo, C. Hu, Adv. Opt. Mater. 10 (6) (2022) 2102018, https://doi.org/10.1002/adom.202102018.
[43] Y. Wu, C. Cao, C. Qiao, Y. Wu, L. Yang, W. Younas, J. Mater. Chem. C 7 (34) (2019) 10613–10622, https://doi.org/10.1039/C9TC03539G.
[44] S. Naghash-Hamed, N. Arsalani, S.B. Mousavi, Sci Rep 13 (1) (2023) 3329, https://doi.org/10.1038/s41598-023-28935-z.
[45] F. Yousefi, S.B. Mousavi, S.Z. Heris, S. Naghash-Hamed, Sci Rep 13 (1) (2023) 7116, https://doi.org/10.1038/s41598-023-34120-z.
[46] W. Gao, Y. Zhou, X. Wu, Q. Shen, J. Ye, Z. Zou, Adv. Funct. Mater. 31 (3) (2021) 2005197, https://doi.org/10.1002/adfm.202005197.
[47] C. Chen, F. Chen, X. Chen, B. Deng, B. Eng, D. Jung, Q. Guo, S. Yuan, K. Watanabe, T. Taniguchi, M.L. Lee, F. Xia, Nano Lett. 19 (3) (2019) 1488–1493, https://doi.org/10.1021/acs.nanolett.8b04041.
[48] M. Ebratkhahan, S. Naghash Hamed, M. Zarei, A. Jafarizad, M. Rostamizadeh, Electrocatalysis 12 (5) (2021) 579–594, https://doi.org/10.1007/s12678-021-00640-3.
[49] E. Kovalska, J. Luxa, T. Hartman, N. Antonatos, P. Shaban, E. Oparin, M. Zhukova, Z. Sofer, Nanoscale 12 (4) (2020) 2638–2647, https://doi.org/10.1039/C9NR10257D.
[50] P. Jakóbczyk, A. Dettlaff, G. Skowierzak, T. Ossowski, J. Ryl, R. Bogdanowicz, Electrochim. Acta 416 (2022), https://doi.org/10.1016/j.electacta.2022.140290.
[51] A. Wieloszyńska, P. Jakóbczyk, R. Bogdanowicz, Low-Dimensional Materials and Devices 2019, Vol. 11085, SPIE, 2019, pp. 84–7.
[52] L. Zhang, B. Wang, Y. Zhou, C. Wang, X. Chen, H. Zhang, Adv. Opt. Mater. 8 (15) (2020) 2000045, https://doi.org/10.1002/adom.202000045.
[53] S. Lange, P. Schmidt, T. Nilges, Inorg. Chem. 46 (10) (2007) 4028–4035, https://doi.org/10.1021/ic062192q.
[54] R.J. Wu, M. Topsakal, T. Low, M.C. Robbins, N. Haratipour, J.S. Jeong, R.M. Wentzcovitch, S.J. Koester, K.A. Mkhoyan, J. Vac. Sci. Technol. A 33 (6) (2015), https://doi.org/10.1116/1.4926753.
[55] S. Smidstrup, T. Markussen, P. Vancraeyveld, J. Wellendorff, J. Schneider, T. Gunst, B. Verstichel, D. Stradi, P.A. Khomyakov, U.G. Vej-Hansen, M.E. Lee, S.T. Chill, F. Rasmussen, G. Penazzi, F. Corsetti, A. Ojanperä, K. Jensen, M.L.N. Palsgaard, U. Martinez, A. Blom, M. Brandbyge, K. Stokbro, J. Phys. Condens. Matter 32 (1) (2020) 36, https://doi.org/10.1088/1361-648X/ab4007.
[56] J.E. Sipe, E. Ghahramani, Phys. Rev. B 48 (16) (1993) 11705–11722, https://doi.org/10.1103/PhysRevB.48.11705.
[57] M.P. Desjarlais, Contrib. Plasma Phys. 45 (3–4) (2005) 300–304, https://doi.org/10.1002/ctpp.200510034.
[58] P.P. Joshi, R. Li, J.L. Spellberg, L. Liang, S.B. King, Nano Lett. 18 (2022) 28, https://doi.org/10.1021/acs.nanolett.1c03849.
[59] X. Ling, S. Huang, E.H. Hasdeo, L. Liang, W.M. Parkin, Y. Tatsumi, A.R.T. Nugraha, A.A. Puretzky, P.M. Das, B.G. Sumpter, D.B. Geohegan, J. Kong, R. Saito, M. Drndic, V. Meunier, M.S. Dresselhaus, Nano Lett. 16 (4) (2016) 2260–2267, https://doi.org/10.1021/acs.nanolett.5b04540.
[60] L. Li, G.J. Ye, V. Tran, R. Fei, G. Chen, H. Wang, J. Wang, K. Watanabe, T. Taniguchi, L. Yang, X.H. Chen, Y. Zhang, Nat. Nanotechnol. 10 (7) (2015) 608–613, https://doi.org/10.1038/nnano.2015.91.
[61] W. Xin, H.B. Jiang, T.Q. Sun, X.G. Gao, S.N. Chen, B. Zhao, J.J. Yang, Z.B. Liu, J.G. Tian, C.L. Guo, Nano Materials Science 1 (4) (2019) 304–309, https://doi.org/10.1016/j.nanoms.2019.09.006.
[62] L. Li, J. Kim, C. Jin, G.J. Ye, D.Y. Qiu, F.H. Da Jornada, Z. Shi, L. Chen, Z. Zhang, F. Yang, K. Watanabe, T. Taniguchi, W. Ren, S.G. Louie, X.H. Chen, Y. Zhang, F. Wang, Nat. Nanotechnol. 12 (1) (2017) 21–25, https://doi.org/10.1038/nnano.2016.171.
[63] A. Favron, E. Gaufrès, F. Fossard, A.L. Phaneuf-Laheureux, N.Y.W. Tang, P.L. Lévesque, A. Loiseau, R. Leonelli, S. Francoeur, R. Martel, Nat. Mater. 14 (8) (2015) 826–832, https://doi.org/10.1038/nmat4299.
[64] Z. Guo, H. Zhang, S. Lu, Z. Wang, S. Tang, J. Shao, Z. Sun, H. Xie, H. Wang, X.F. Yu, P.K. Chu, Adv. Funct. Mater. 25 (45) (2015) 6996–7002, https://doi.org/10.1002/adfm.201502902.
[65] W. Lu, H. Nan, J. Hong, Y. Chen, C. Zhu, Z. Liang, X. Ma, Z. Ni, C. Jin, Z. Zhang, S.-V. Berlin, (n.d.). 10.1007/s12274-014-0446-7.
[66] A. Dettlaff, G. Skowierzak, MacEwicz, M. Sobaszek, J. Karczewski, M. Sawczak, J. Ryl, T. Ossowski, R. Bogdanowicz, Journal of Physical Chemistry C 123(33) (2019) 20233–40. 10.1021/acs.jpcc.9b03028.
[67] A. Castellanos-Gomez, L. Vicarelli, E. Prada, J.O. Island, K.L. Narasimha-Acharya, S.I. Blanter, D.J. Groenendijk, M. Buscema, G.A. Steele, J.V. Alvarez, H.W. Zandbergen, J.J. Palacios, H.S.J. van der Zant, 2D Mater. 1(2) (2014) 025001. 10.1088/2053-1583/1/2/025001.
[68] J.A.W. Company, Guide to Using WVASE32, Vol. 30, New York, 2010.
[69] H. Fujiwara, Spectroscopic Ellipsometry: Principles and Applications, New York, 2007.
[70] S.-Y. Lee, K.-J. Yee, 2D Mater. 9 (1) (2021), https://doi.org/10.1088/2053-1583/ac3a99.
[71] J. Jia, Y. Ban, K. Liu, L. Mao, Y. Su, M. Lian, T. Cao, Adv. Opt. Mater. 9 (16) (2021) 1–7, https://doi.org/10.1002/adom.202100499.
[72] V. Tran, R. Soklaski, Y. Liang, L. Yang, Physical Review B - Condensed Matter and Materials Physics 89 (23) (2014), https://doi.org/10.1103/PhysRevB.89.235319.
[73] R. Kochar, S. Choudhary, IEEE J. Quantum Electron. 54 (2018) 4, https://doi.org/10.1109/JQE.2018.2850450.
[74] V. Tran, L. Yang, Physical Review B - Condensed Matter and Materials Physics 89 (24) (2014), https://doi.org/10.1103/PhysRevB.89.245407.
[75] Y. Liu, M. Bo, X. Yang, P. Zhang, C.Q. Sun, Y. Huang, PCCP 19 (7) (2017) 5304–5309, https://doi.org/10.1039/c6cp08011a.
[76] V.A. Saroka, I. Lukyanchuk, M.E. Portnoi, H. Abdelsalam, Phys. Rev. B 96 (8) (2017) 85436, https://doi.org/10.1103/PhysRevB.96.085436.
[77] Y. Mogulkoc, M. Modarresi, A. Mogulkoc, Y.O. Ciftci, Comput. Mater. Sci 124 (2016) 23–29, https://doi.org/10.1016/j.commatsci.2016.07.015.
[78] H. Sarwar, P. Ji, S. Shafique, X. Wang, S. Yang, RSC Adv. 13 (2) (2023) 1223–1228, https://doi.org/10.1039/d2ra06504e.
[79] G. Tiouitchi, M.A. Ali, A. Benyoussef, M. Hamedoun, A. Lachgar, A. Kara, A. Ennaoui, A. Mahmoud, F. Boschini, H. Oughaddou, A. El Moutaouakil, A. El Kenz, O. Mounkachi, R. Soc. Open Sci. 7 (2020) 10, https://doi.org/10.1098/rsos.201210.
[80] F. Luo, D. Wang, J. Zhang, X. Li, D. Liu, H. Li, M. Lu, X. Xie, L. Huang, W. Huang, ACS Applied Nano Materials 2 (6) (2019) 3793–3801, https://doi.org/10.1021/acsanm.9b00667.
[81] B. Tian, B. Tian, B. Smith, M.C. Scott, Q. Lei, R. Hua, Y. Tian, Y. Liu, PNAS 115 (17) (2018) 4345–4350, https://doi.org/10.1073/pnas.1800069115.
[82] A.H. Woomer, T.W. Farnsworth, J. Hu, R.A. Wells, C.L. Donley, S.C. Warren, ACS Nano 9 (9) (2015) 8869–8884, https://doi.org/10.1021/acsnano.5b02599.
[83] H. Jiang, H. Shi, X. Sun, B. Gao, ACS Photonics 5 (6) (2018) 2509–2515, https://doi.org/10.1021/acsphotonics.8b00341.
[84] H. Asahina, A. Morita, J. Phys. C: Solid State Phys. 17 (11) (1984) 1839, https://doi.org/10.1088/0022-3719/17/11/006.
[85] C. Li, Z. Xie, Z. Chen, N. Cheng, J. Wang, G. Zhu, Materials 11 (2) (2018) 304, https://doi.org/10.3390/ma11020304.
[86] R. Schuster, J. Trinckauf, C. Habenicht, M. Knupfer, B. Büchner, Phys. Rev. Lett. 115 (2) (2015), https://doi.org/10.1103/PhysRevLett.115.026404.
[87] A. Islam, W. Du, V. Pashaei, H. Jia, Z. Wang, J. Lee, G.J. Ye, X.H. Chen, P.X.L. Feng, ACS Appl. Mater. Interfaces 10 (30) (2018) 25629–25637, https://doi.org/10.1021/acsami.8b05408.
[88] W.S. Whitney, M.C. Sherrott, D. Jariwala, W.H. Lin, H.A. Bechtel, G.R. Rossman, H.A. Atwater, Nano Lett. 17 (1) (2020) 78–84, https://doi.org/10.1021/acs.nanolett.6b03362.